

# Supporting Information

## Diagnosing Ozone-NO<sub>x</sub>-VOCs-Aerosols Sensitivity to Uncover Urban-nonurban Discrepancies in Shandong, China using Transformer-based High-resolution Air Pollution Estimations

*Chenliang Tao<sup>1</sup>, Yanbo Peng<sup>1,2,\*</sup>, Qingzhu Zhang<sup>1,\*</sup>, Yuqiang Zhang<sup>1</sup>, Bing  
Gong<sup>3</sup>, Qiao Wang<sup>1</sup>, Wenxing Wang<sup>1</sup>*

<sup>1</sup>Big Data Research Center for Ecology and Environment, Environmental Research  
Institute, Shandong University, Qingdao 266237, P.R. China

<sup>2</sup>Shandong Academy for Environmental Planning, Jinan 250101, P. R. China

<sup>3</sup>Jülich Supercomputing Centre, Forschungszentrum Jülich, 52425 Jülich, Germany

### **Keywords:**

Air pollution, Deep learning, Transformer, Satellite, Urban-rural difference, Ozone Regime

## 26 **Text S1 Variables Selected**

27 Satellite data have been extensively used to derive surface air pollutant concentration<sup>1,2</sup>. The daily  
28 tropospheric NO<sub>2</sub> vertical column densities (VCDs) and O<sub>3</sub> total VCDs with a horizontal resolution  
29 of 5.5 × 3.5 km<sup>2</sup> were measured by TROPOMI. The daily AOD data and atmospheric properties  
30 with a 1 km resolution were obtained from MODIS Terra and Aqua combined multiangle  
31 implementation of atmospheric correction (MAIAC) land AOD product (MCD19A2)<sup>3</sup>. In addition,  
32 we used AOD estimates from the Modern-Era Retrospective Analysis for Research and Applications,  
33 version 2 (MERRA-2) as the supplement of MODIS for filling extensively missing values. The  
34 meteorological reanalysis data were obtained from the fifth generation ECMWF reanalysis for the  
35 global climate and weather (ERA5) hourly products<sup>4</sup>. Ancillary data related to human activity and  
36 geographical information were retrieved and rasterized, including daily dynamic industrial  
37 emissions, moonlight-adjusted nighttime lights (NTL) product, population density, road density,  
38 land use data, the shuttle radar topography mission digital elevation model (DEM), the MOD13Q1  
39 vegetation index (VI) product, and the MOD11A1 land surface temperature (LST) product.  
40 Industrial emissions amount (unit: kg) contains three categories, i.e. sulfur dioxide (SO<sub>2</sub>), NO<sub>x</sub>, and  
41 particulate matter (PM), collected from SDEM. Geographic covariates directly related to pollution  
42 emissions, such as industrial emission, and road density were decomposed into magnitude-related  
43 data by using Gaussian convolution kernels to account for the impact of neighboring sources (Text  
44 S2).

## 45 **Text S2 Data Extension of Emission Proxies**

46 The procedure of data extension follows from a previous study<sup>5</sup>, geographic covariates directly  
47 related to pollution emissions like industrial emission, road density, and population density were  
48 decomposed into magnitude-related data by using Gaussian convolution kernels to account for the  
49 impact of neighboring sources. In this study, after rasterizing all spatial data to match with the tarterd  
50 grid, the Gaussian convolution with the size of width (ranging from 1.5 to 31.5 km) was used to  
51 consider the impact of nearby sources. For the Gaussian convoluted values with various at each  
52 location, the maximum value () was assigned as the characteristic magnitude of the emission proxy  
53 map for describing the influence of potential air pollution emission.

## 54 **Text S3 Spatiotemporal Proxies**

55 Taking the space-time-variant into consideration, three Euclidean spherical coordinates (eqs 1 –  
56 3) and three helix-shape trigonometric sequences (eqs 4 – 6) were calculated as following:<sup>6</sup>

$$57 \quad s_1 = \cos\left(2\pi \frac{longitude}{360}\right) \cos\left(2\pi \frac{latitude}{180}\right) \quad (1)$$

$$58 \quad s_2 = \cos\left(2\pi \frac{longitude}{360}\right) \sin\left(2\pi \frac{latitude}{180}\right) \quad (2)$$

$$59 \quad s_3 = \sin\left(2\pi \frac{longitude}{360}\right) \quad (3)$$

$$60 \quad \cos\_sea = \cos\left(2\pi \frac{month}{12}\right) \quad (4)$$

$$61 \quad \sin\_sea = \sin\left(2\pi \frac{month}{12}\right) \quad (5)$$

$$62 \quad \cos\_mon = \frac{month}{360} \quad (6)$$

## 63 **Text S4 Data Fusion and Gap filling**

64 Due to the various data sources and types, we bilinearly interpolated predictor variables to the  
65 targeted grid with 500 m resolution to harmonize with other data. The daily Ozone (O<sub>3</sub>), fine  
66 particulate matter (PM<sub>2.5</sub>) and nitrogen dioxide (NO<sub>2</sub>) concentrations were assigned to their overlay  
67 cells by spatial aggregation.

68 The detection of trace gases information below-cloud was prevented by the shielding of ubiquitous  
69 clouds in optical remote sensing images, causing the existence of gaps in satellite productions. We  
70 utilize the efficient machine-learning model, called Light Gradient Boosting Machine (LightGBM)<sup>7</sup>,  
71 to fill the gaps in satellite data. LightGBM is designed to be distributed and efficient with the  
72 advantages of faster training speed and higher accuracy. Thus, it can impute a large dataset (1407 ×  
73 863 grids in the targeted resolution) with missing data in multiple variables using an iterative way.  
74 For each iteration, available daily satellite-based data are regarded as the observations, and the  
75 missing values are predicted by the LightGBM with meteorological reanalysis and geographical  
76 coordinates. The number of iterations corresponds to the number of satellite products with missing  
77 values. Here, the satellite-based production contains MOIDS AOD, TROPOMI NO<sub>2</sub> and O<sub>3</sub> column  
78 density, normalized difference vegetation index (NDVI); enhanced vegetation index (EVI), and land  
79 surface temperature (LST). Applying the model of filling missing values, the predictions of all

80 variables are reliable, with the average coefficient of determination ( $R^2$ ) values ranging from 0.87  
81 to 0.99 in the validation set.

## 82 **Text S5 The Detail of Air Transformer (AiT)**

83 In this study,  $V, T, H$  and  $W$  are configured to 57, 8, 5 and 5, respectively, according to the number  
84 of chosen variables and the empirical range of time and spatial. The data size remains unchanged  
85  $V \times 8 \times 5 \times 5$  for the first AiT encoder blocks, while for the next 3 blocks, 2 blocks, and 1  
86 block, the temporal dimensions and spatial window size are reduced by the convolutional embedded  
87 block, which includes convolution operation with  $2 \times 2 \times 2$  filter with the stride of  $2 \times 1 \times 1$ ,  
88 and the number of variables' channels is 64, 96 and 128, resulting in data size of  $64 \times 4 \times 4 \times 4$ ,  
89  $96 \times 2 \times 3 \times 3$  and  $128 \times 1 \times 2 \times 2$ . The data dimensionality is transformed through a  
90 linear layer in decoder blocks.

91 We train AiT via backpropagation using an AdamW optimizer with a learning strategy of warmup,  
92 a learning rate of 0.0005 and a batch size of 256, and apply early stopping on the validation loss  
93 using patience of 300 epochs. we combat overfitting by dropout within each layer of linear and self-  
94 attention. A GeLU activation function is applied throughout the network. The loss function of mean  
95 squared error was applied to the errors for the computation of gradients in the optimization. The  
96 model is coded and trained using the Pytorch library. Before the data is fed into the model for  
97 training, it is normalized over the entire dataset. The total dataset for training and testing has  
98 262,656 instances.

99 For sensitivity analysis, we first simply applied the image and video recognition Transformers for  
100 the estimation and also achieved good prediction performance ( $R^2$  of 0.96 for  $O_3$  in Timesformer).  
101 However, the spatial distribution of estimation exhibits severe “reticular phenomenon” (Figure S5).  
102 We briefly analyze the reasons why original Transformer-based models fell into trouble in terms of  
103 pollutant maps. Firstly, these original Transformer-based image models are purely based on pixel  
104 units for self-attention computation. Air pollution estimation often involves various features  
105 (satellite, meteorological, and emission proxies, etc.)<sup>2,8-10</sup>, which is unlike image data with just  
106 three channels (red, green, and blue). These models overly focus on the correlation between  
107 neighboring grids and lack extraction of deep features, resulting in a discontinuous distribution of

108 estimation for our study. Secondly, they paid attention to the full domain of pixels and there were  
 109 no overlaps between samples, so only the encoder part of Transformer was used. Air quality  
 110 estimation could be troubled by the overlearning of neighborhood features and extensive data  
 111 duplication of adjacent samples when existing deep learning models are directly applied.  
 112 Summarizing the above factors, we believe that it is necessary to build upon a tradeoff between the  
 113 spatial distribution of estimations and the performance of the model.

## 114 **Text S6 Multi-task Learning Strategy**

115 It not only leverages large amounts of cross-task data but also benefits from a regularization effect  
 116 that leads to more general representations to help adapt to estimating multiple pollutants  
 117 simultaneously and efficiently,<sup>11</sup> and alleviating overfitting to a specific pollutant. As shown in the  
 118 bottom right of Figure 1, the encoder and decoder blocks are shared across all predictions, while the  
 119 last block is task-specific combining different estimations of PM<sub>2.5</sub>, O<sub>3</sub>, and NO<sub>2</sub>. The shared blocks  
 120 can take advantage of the interrelationship between different air pollutants by learning the intrinsic  
 121 features of data. The task-specific blocks can capture the relevant information needed for the single  
 122 task from extracted potential features of Transformer blocks.

## 123 **Text S7 Method: Inferring Surface HCHO**

### 124 **Column-to-surface Conversion Factor**

125 The satellite-derived surface HCHO concentrations ( $S_g$ ) from Tropospheric Ozone Monitoring  
 126 Instrument (TROPOMI) formaldehyde (HCHO) vertical columns density (VCD) by the simulated  
 127 surface-to-column conversion factor method described in literatures<sup>12,13</sup>:

$$128 \quad S_g = \frac{vV_M - V_M^{upper}}{V_M^{lower}} \times \frac{S_M}{V_M} \times V_g^- \quad (7)$$

129 where,  $S_g$  is the inferred surface level HCHO mixing ratio,  $S_M$  and  $V_M$  are the surface and  
 130 tropospheric HCHO concentration,  $V_M^{lower}$  is the lower partial column,  $V_M^{upper}$  is the upper partial  
 131 columns simulated by the CAM-Chem chemical transport model,  $V_g^-$  is the averaged tropospheric  
 132 TROPOMI HCHO VCD within the WRF-model, and  $v$  represents the satellite-observed sub-  
 133 model-grid spatial variability calculated as:

$$134 \quad v = \frac{V_g}{V_g^-} \quad (8)$$

135 where  $V_g$  is the tropospheric HCHO VCD in the TROPOMI grid. HCHO below the lower layer is  
136 considered to be well mixed in the vertical direction, and a large portion of HCHO (~70%) appears  
137 over the boundary layer, causing a nonhomogeneous distribution of upper partial columns.  
138 Therefore, in this study, the altitude where the HCHO partial column reaches the half maximum of  
139 its profile is regarded as the lower layer, following a previous study<sup>12</sup>.

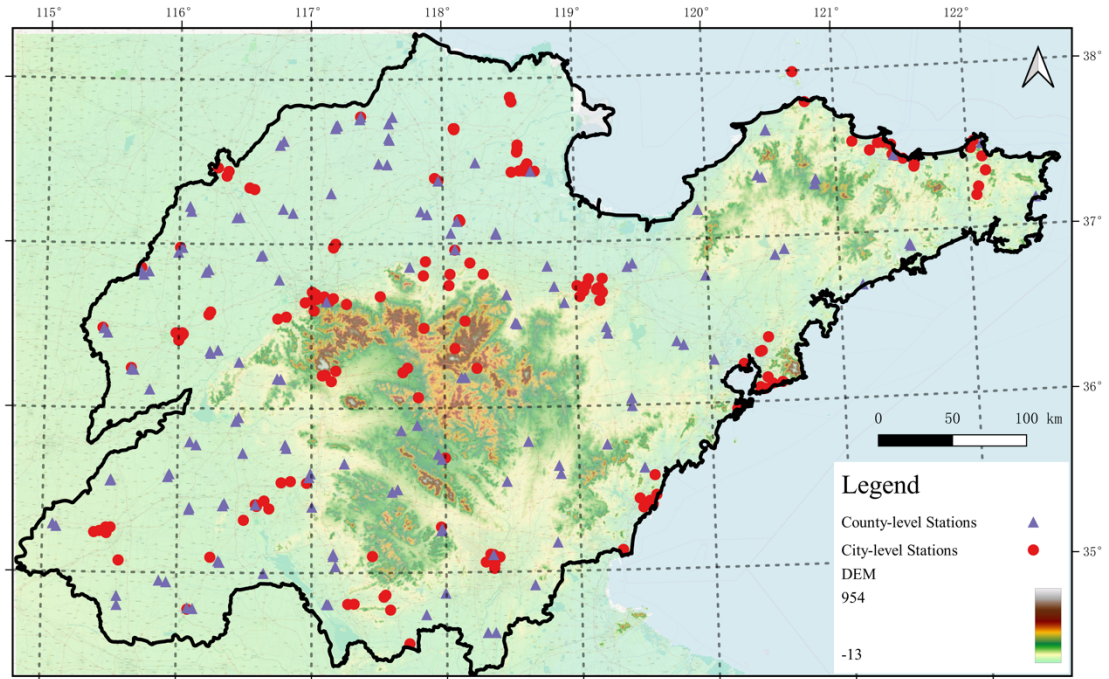
#### 140 **ECMWF Atmospheric Composition Reanalysis 4 (EAC4)**

141 To derive the surface HCHO concentration, we used the European Centre for Medium-Range  
142 Weather Forecasts (ECMWF) Atmospheric Composition Reanalysis 4 (EAC4) at 0.75×0.75  
143 horizontal resolution simulation with 25 vertical levels.<sup>14</sup> Reanalysis combines model data with  
144 observations from across the world into a globally complete and consistent dataset using a model of  
145 the atmosphere based on the laws of physics and chemistry. The monthly averaged field of EAC4  
146 was used in our study.

#### 147 **Text S8 Cross Validation**

148 The performance of our AiT model is evaluated through two cross-validation (CV) methods: out-  
149 of-sample 10-fold CV and out-of-site 10-fold CV. The out-of-sample CV, where all samples are  
150 randomly divided into 10 folds, saving one-fold for testing, is widely used for comparing  
151 measurements with the predictions of the out-of-bag sample. In addition, the generalization  
152 capability of spatial prediction at the location without monitors is evaluated by out-of-site CV, which  
153 randomly divides all sites into 10 subsets and then trains the model using four subsets and tests the  
154 model on the remaining subset.

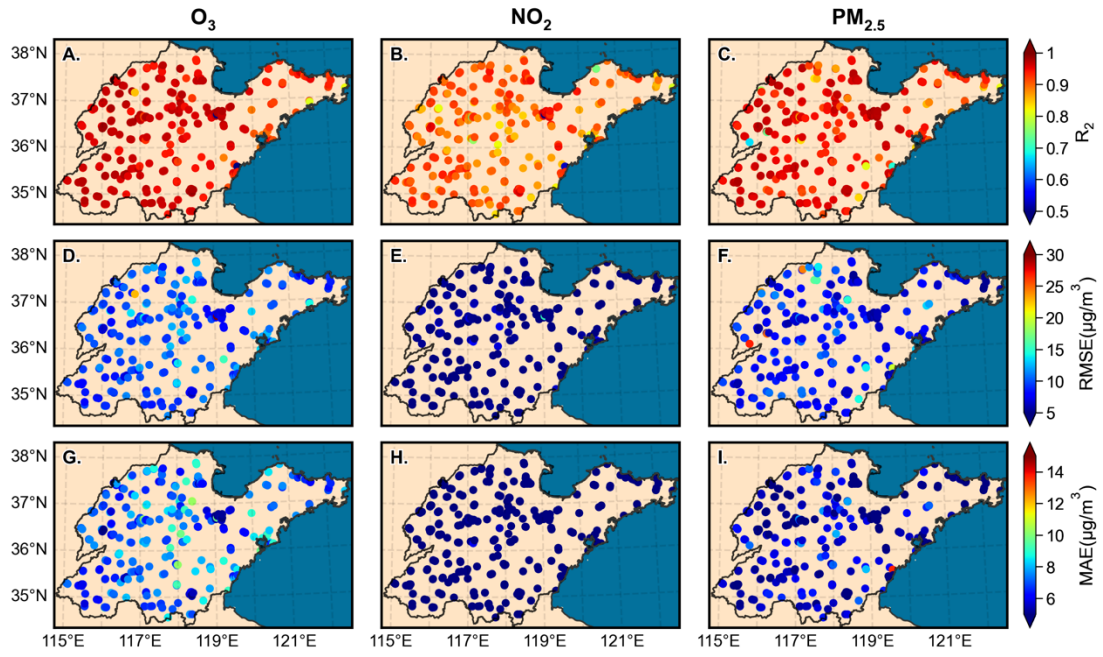
155



156

157 **Figure S1.** Map of study domain and location of monitoring stations. Purple triangles  
 158 show the county-level air quality monitoring stations from SDEM, and red markers  
 159 show the city-level air quality monitoring stations from CNEMC. The base map is the  
 160 overlay of the © Google Maps and Digital Elevation Model (DEM) data.

161



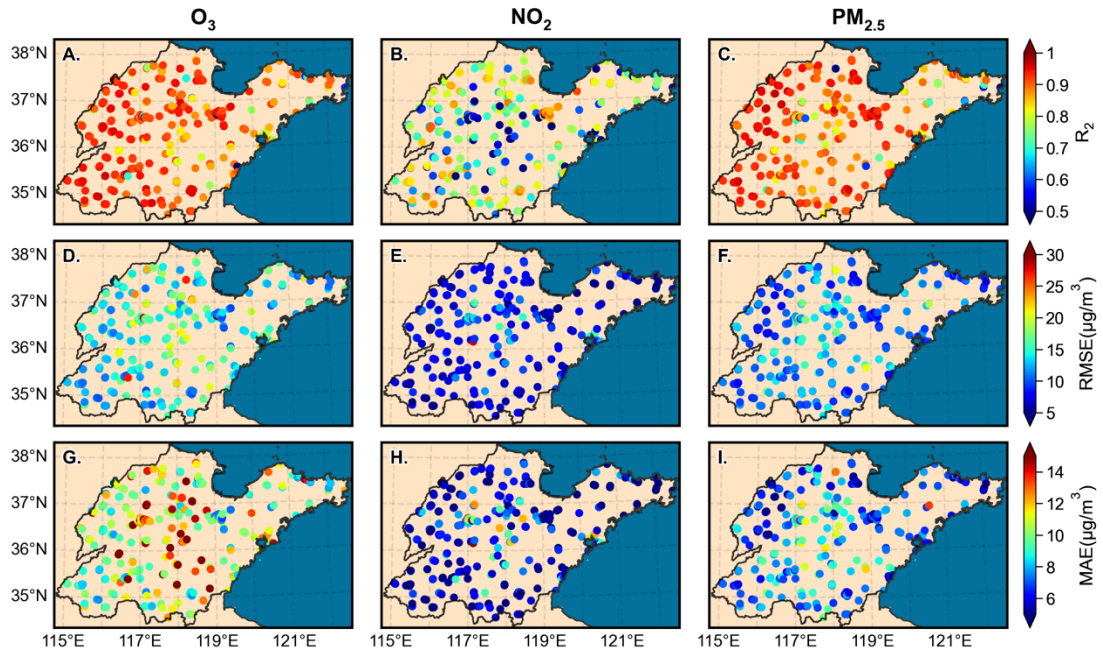
162

163 **Figure S2.** Out-of-sample cross-validation of daily surface  $O_3$ ,  $NO_2$  and  $O_3$  estimates

164 at each monitoring site.

165



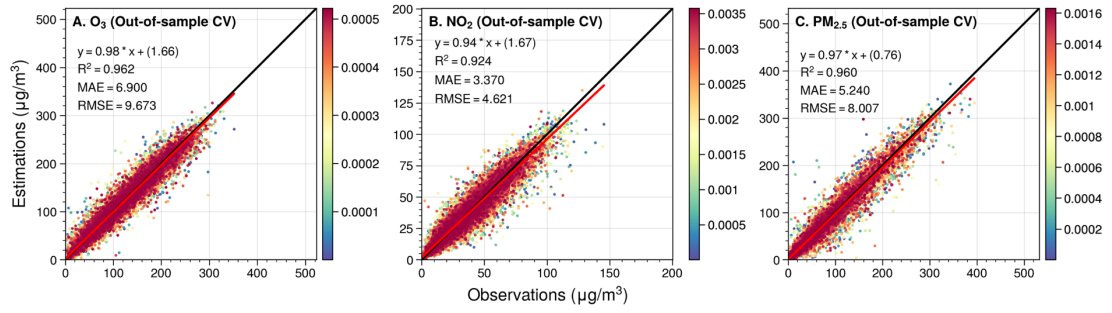


166

167 **Figure S3.** Out-of-site cross-validation of daily surface  $O_3$ ,  $NO_2$  and  $O_3$  estimates at

168 each monitoring site.

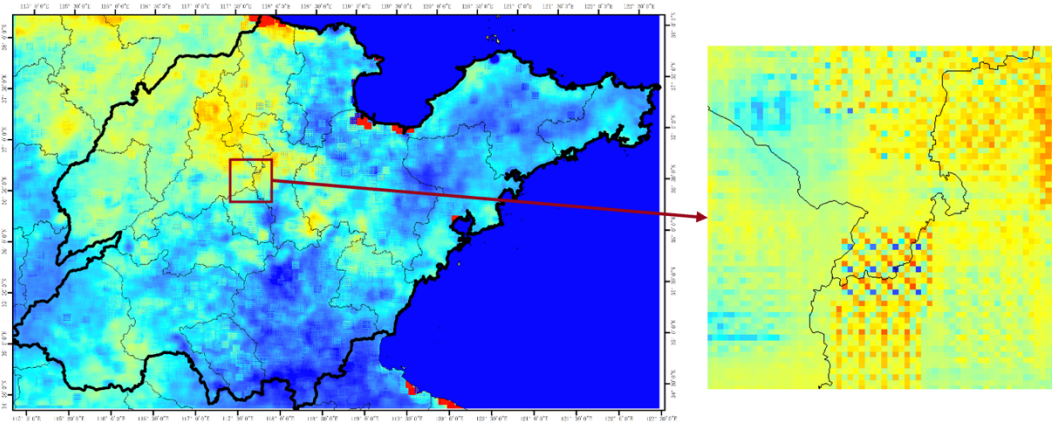
169



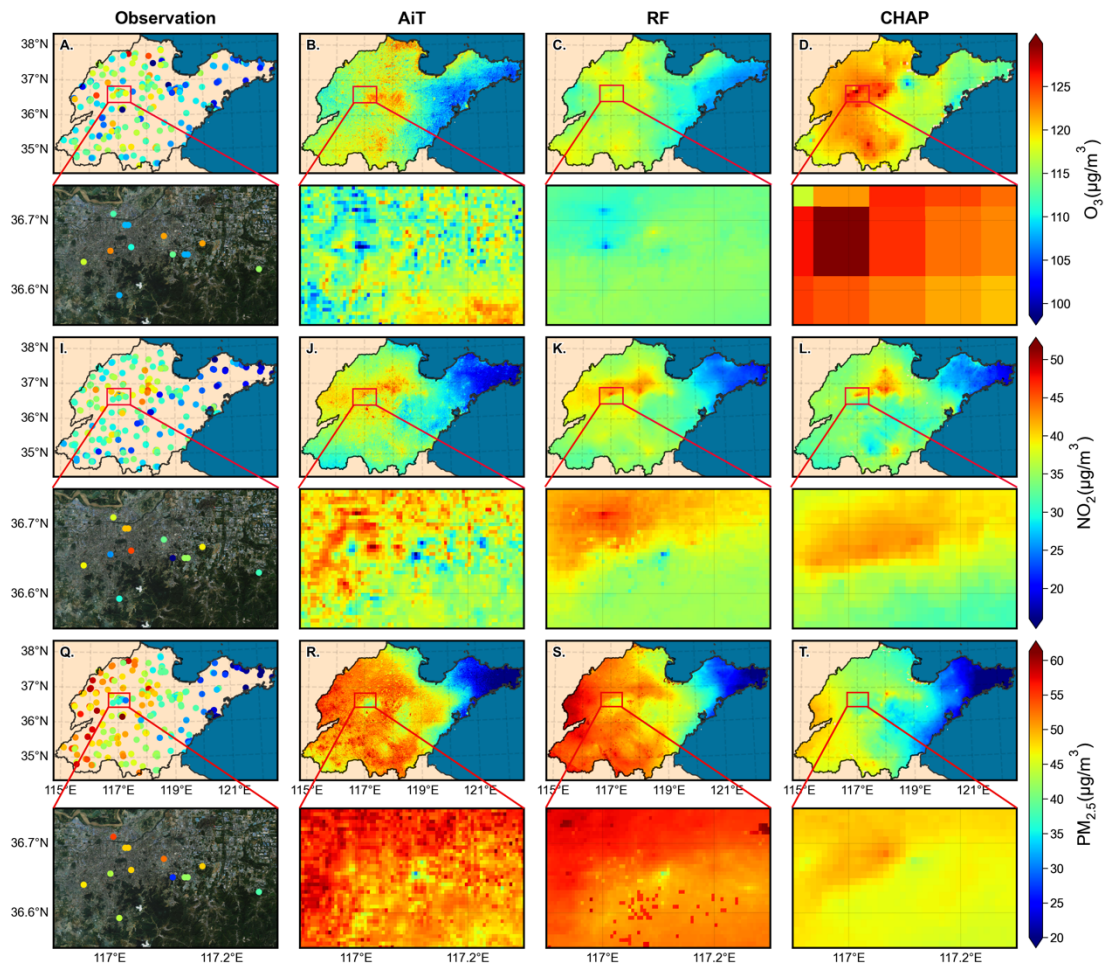
170

171 **Figure S4.** Out-of-sample cross-validation (A-C) of daily ground-level O<sub>3</sub>, NO<sub>2</sub> and  
 172 PM<sub>2.5</sub> concentration in the validation set based on the AiT model trained by monitoring  
 173 data of CNEMC.

174



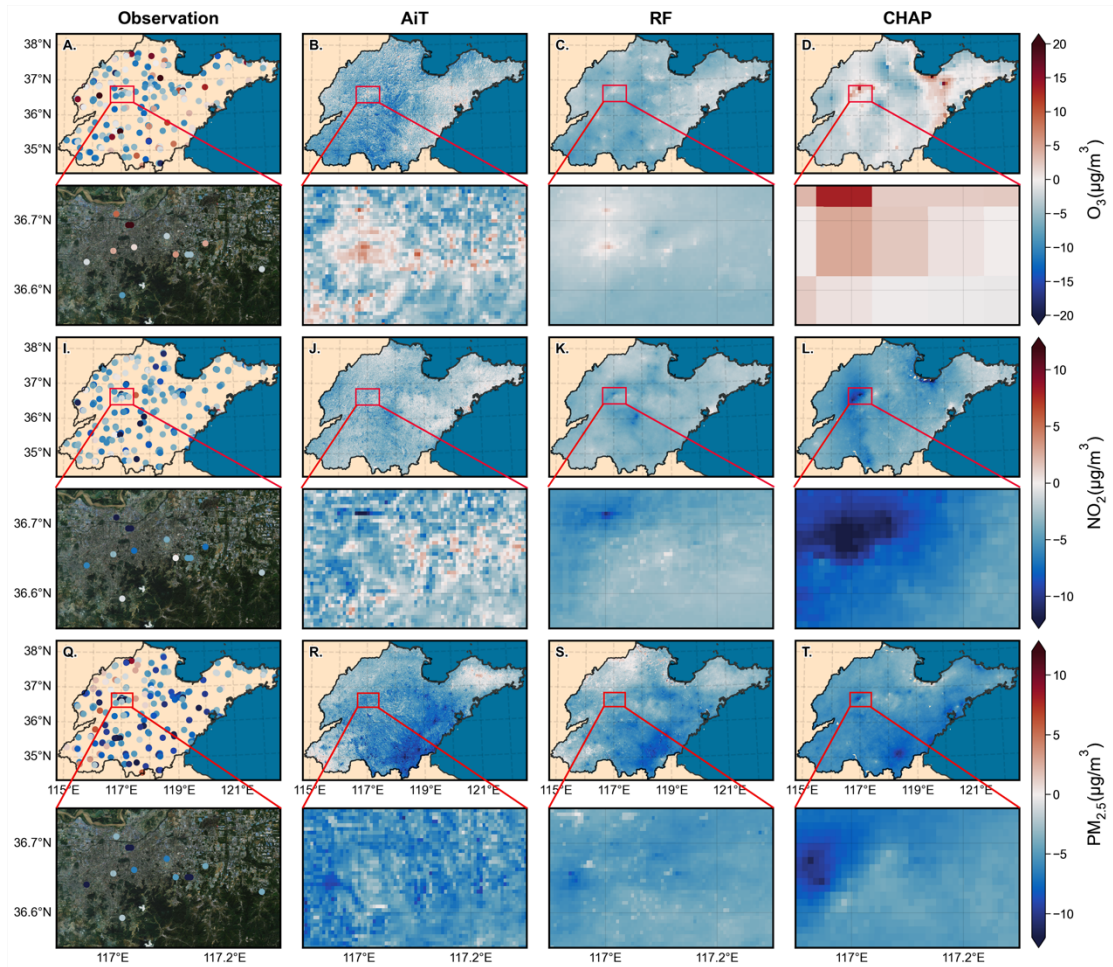
175  
176 **Figure S5.** The estimated O<sub>3</sub> concentration on May 12, 2018, in Shandong, China using  
177 Timesformer (left) and also the zoomed-in map in region-scale distribution (right). The  
178 blue area represents the ocean.  
179



180

181 **Figure S6.** Spatial distribution of the annual mean (A-D) O<sub>3</sub>, (I-L) NO<sub>2</sub> and (Q-T) PM<sub>2.5</sub>  
 182 concentrations from observations, Air Transformer (AiT), Random Forest (RF) and  
 183 ChinaHighAirPollutants (CHAP), respectively, in 2020. The region enclosed by the red  
 184 rectangular box in (A-T) corresponds to the zoomed-in maps of satellite (© Tianditu:  
 185 www.tianditu.gov.cn) and pollutant concentrations at a city scale for the capital city of  
 186 Shandong Province, Jinan.

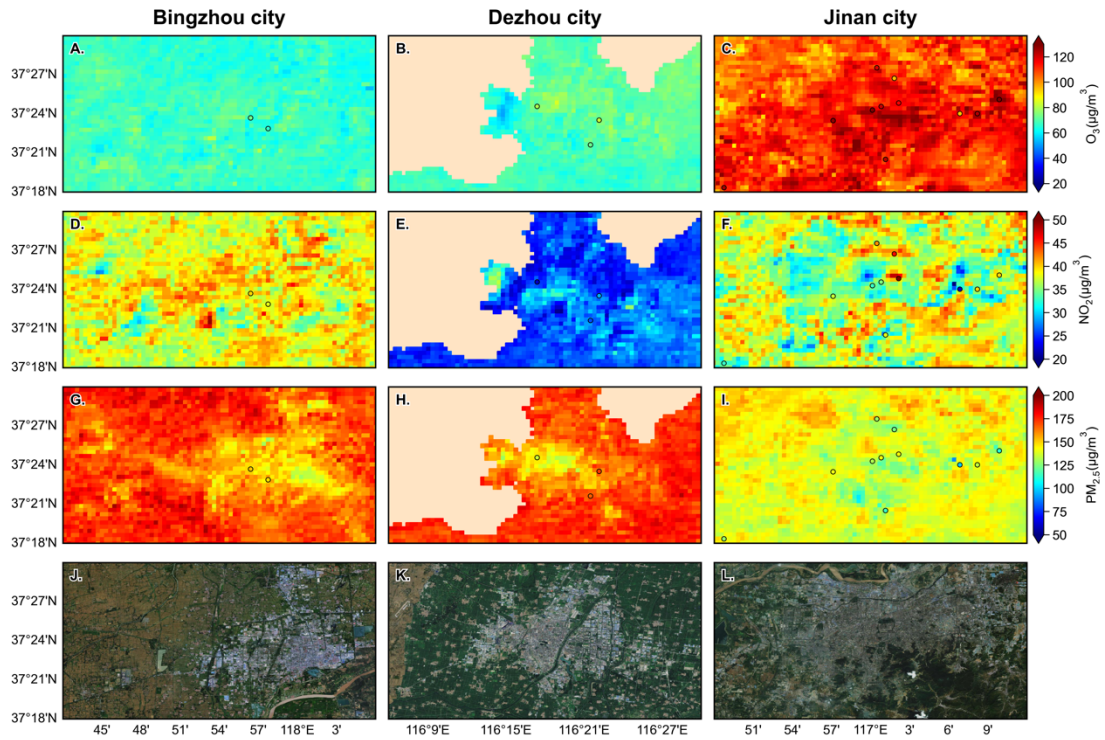
187



188

189 **Figure S7.** Spatial distribution of annual mean disparities for (A-D) O<sub>3</sub>, (I-L) NO<sub>2</sub> and  
 190 (Q-T) PM<sub>2.5</sub> concentrations from observations, Air Transformer (AiT), Random Forest  
 191 (RF) and ChinaHighAirPollutants (CHAP), respectively, during 2019-2020. The region  
 192 enclosed by the red rectangular box in (A-T) corresponds to the zoomed-in maps of  
 193 satellite (© Tianditu: [www.tianditu.gov.cn](http://www.tianditu.gov.cn)) and pollutant concentrations at a city scale  
 194 for the capital city of Shandong Province, Jinan.

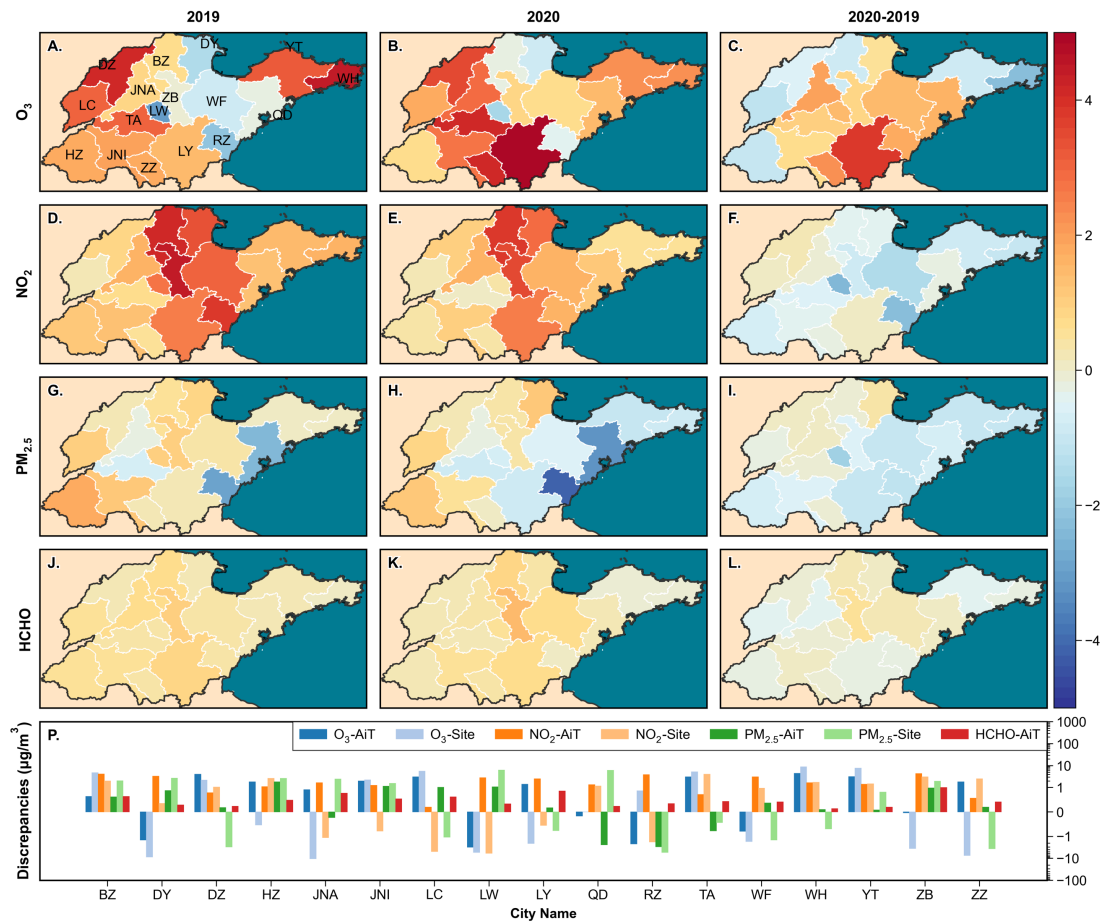
195



196

197 **Figure S8.** The spatial distribution of ground-level O<sub>3</sub> (A-C), NO<sub>2</sub> (D-F), and PM<sub>2.5</sub> (G-  
 198 I) from AiT and monitoring stations in three cities experiencing diverse dust storm  
 199 pollution on 15 March 2021 in Shandong, China. J-L represents the satellite maps of  
 200 these cities (© Tianditu: [www.tianditu.gov.cn](http://www.tianditu.gov.cn)).

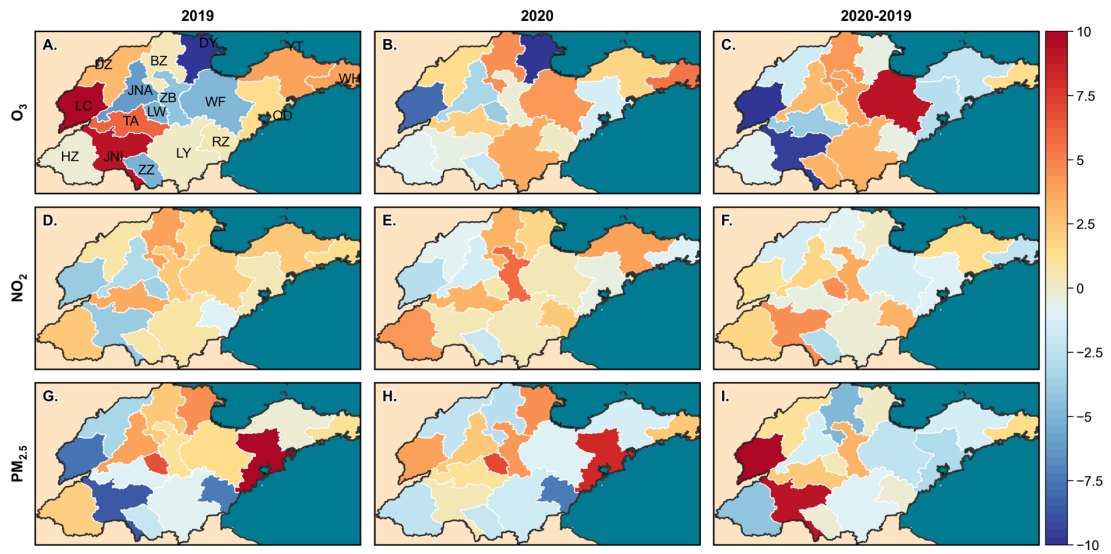
201



202

203 **Figure S9.** The urban-nonurban disparities of O<sub>3</sub>, NO<sub>2</sub>, PM<sub>2.5</sub> and HCHO calculated by  
 204 AiT across cities with administrative divisions in Shandong, China during summer in  
 205 2019 (A, D, G) and 2020 (B, E, H), and the changes of differences between 2019 and  
 206 2020 (C, F, I).

207

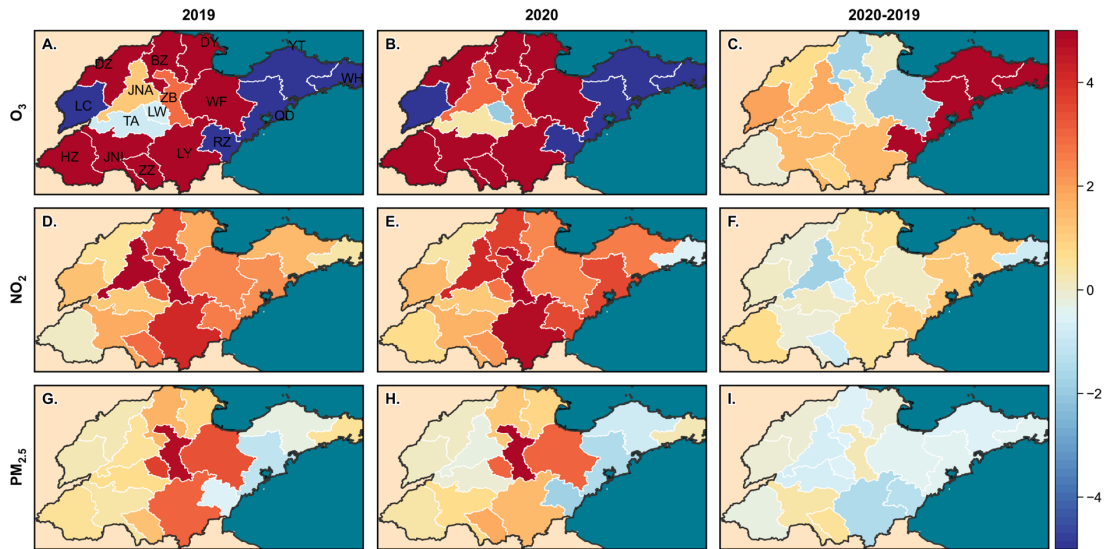


209

210 **Figure S10.** The urban-nonurban disparities of  $O_3$ ,  $NO_2$ , and  $PM_{2.5}$  were calculated by  
 211 monitoring station data across cities in Shandong, China in 2019 (A, D, G) and 2020  
 212 (B, E, H), and the changes of differences between 2019 and 2020 (C, F, I).

213

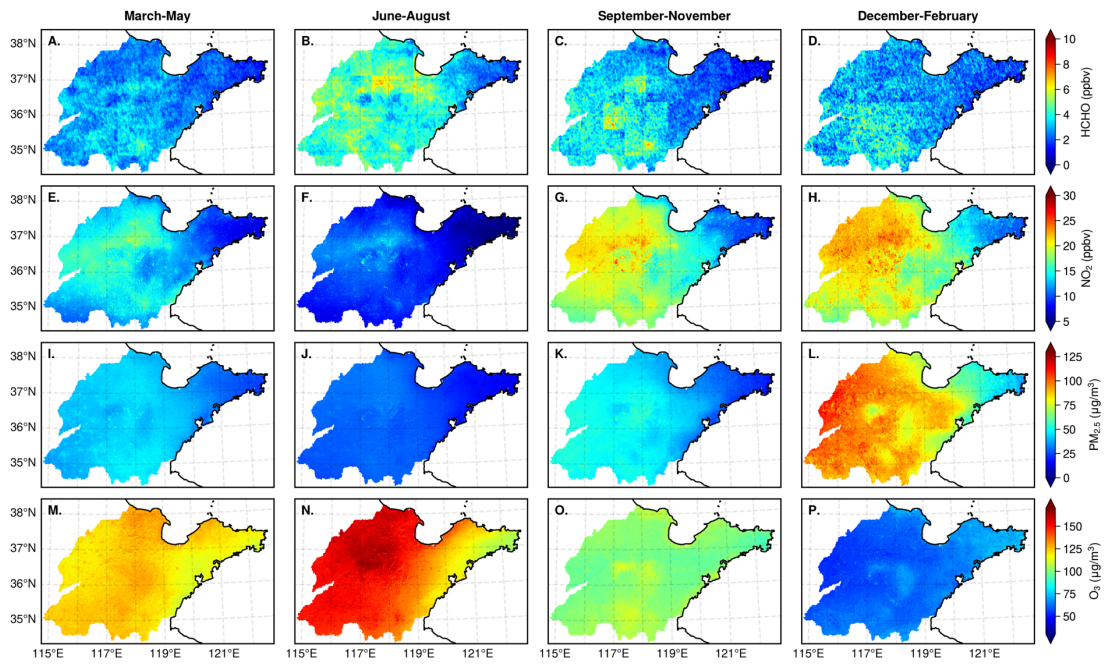




214

215 **Figure S11.** The urban-nonurban disparities of O<sub>3</sub>, NO<sub>2</sub>, and PM<sub>2.5</sub> calculated by CHAP  
 216 across cities in Shandong, China in 2019 (A, D, G) and 2020 (B, E, H), and the changes  
 217 of differences between 2019 and 2020 (C, F, I).

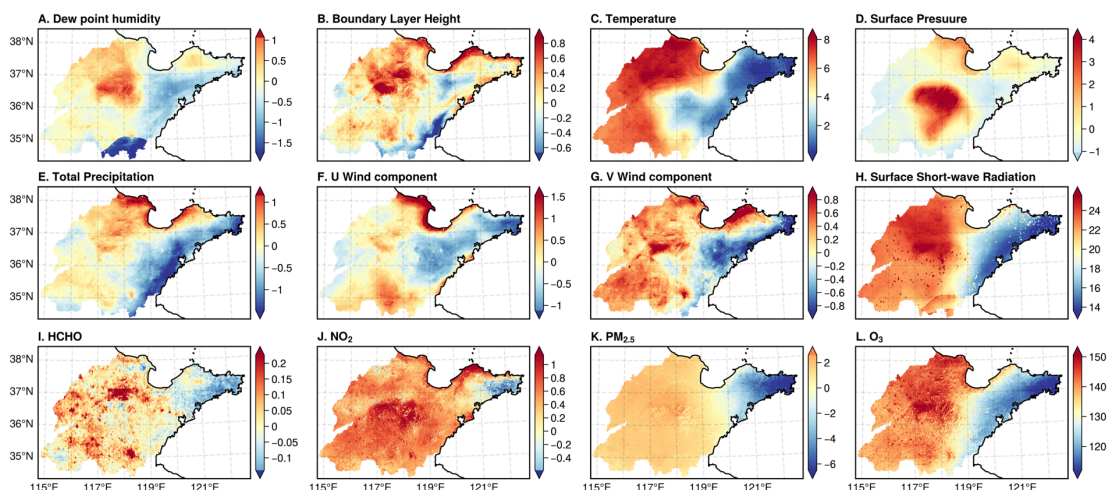
218



219

220 **Figure S12.** The seasonal changes of surface HCHO mixing ratio inferred from  
 221 TROPOMI and EAC4 (A-D), and surface NO<sub>2</sub> (E-D), PM<sub>2.5</sub> (I-L) and O<sub>3</sub> (M-P) derived  
 222 from Air Transformer across Shandong, China, in 2010 and 2020.

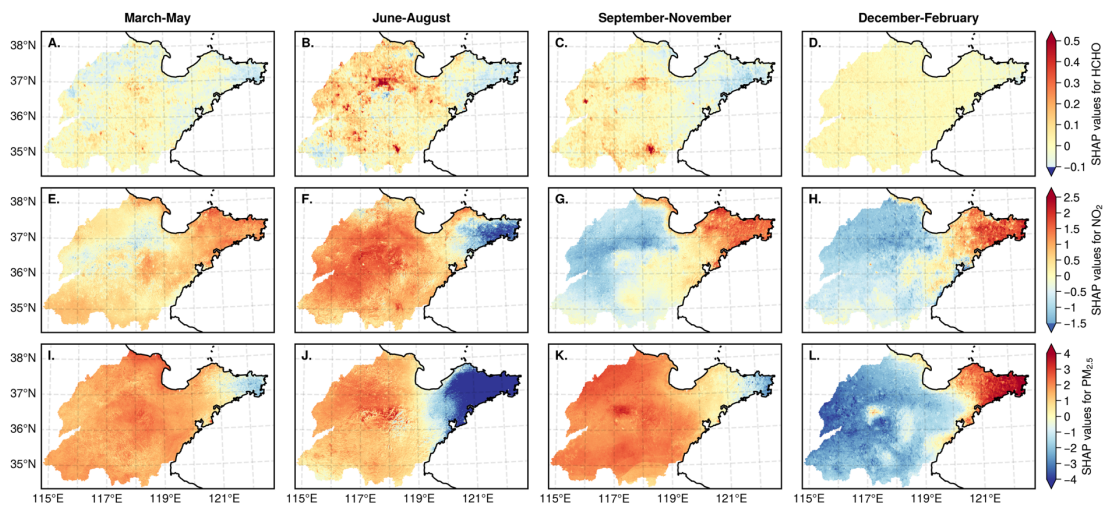
223



224

225 **Figure S13.** The geographical distribution of the averaged SHAP values for the  
 226 important driving factors of O<sub>3</sub> production (A-K) in XGBoost model, and O<sub>3</sub>  
 227 concentration (L) from May to October across Shandong, China in 2019 and 2020. The  
 228 above color demonstrates how different variables each contribute to pushing the model  
 229 output away from the base value (the average model output over the training dataset)  
 230 towards the actual model output. Variables pushing the O<sub>3</sub> higher are shown in red,  
 231 indicating they promote O<sub>3</sub> formation. In contrast, variables pushing the estimations  
 232 lower are in blue, revealing they inhibit O<sub>3</sub> formation.

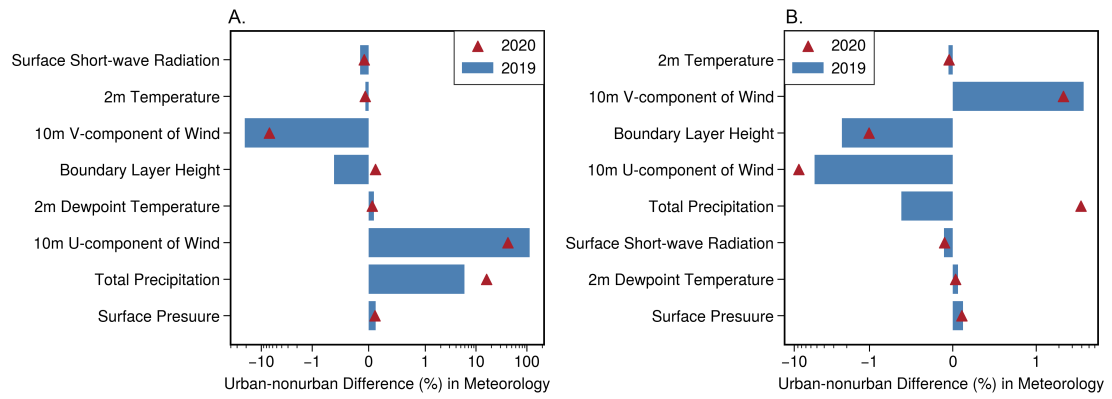
233



234

235 **Figure S14.** The seasonal changes of SHAP values in HCHO (A-D), NO<sub>2</sub> (E-H) and  
 236 PM<sub>2.5</sub> (I-L) for O<sub>3</sub> formation across Shandong, China in 2019 and 2020.

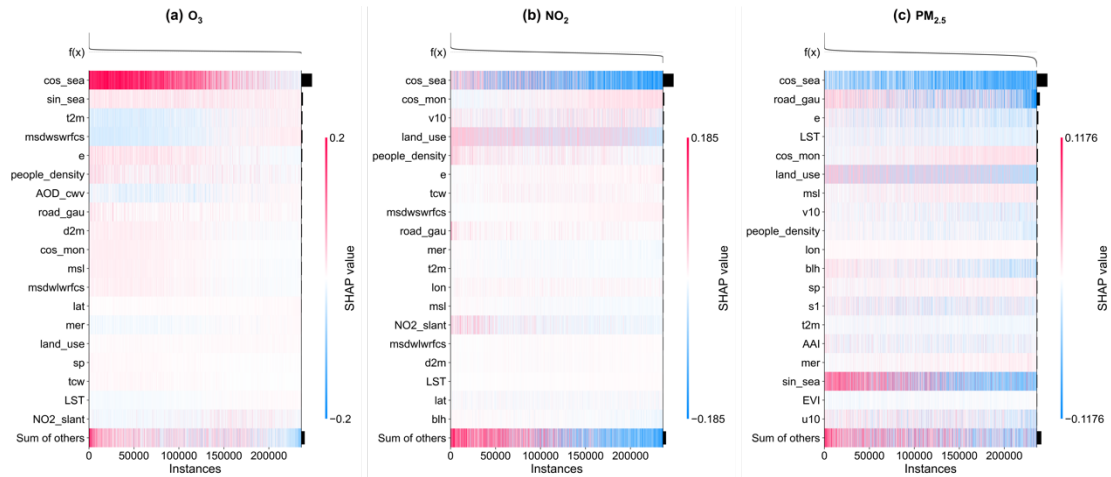
237



238

239 **Figure S15.** The changes in urban-nonurban discrepancies of meteorological  
 240 conditions between 2019 and 2020 in Shandong, China during the lockdown periods  
 241 (A) and summertime (B).

242



243

244 **Figure S16.** Contribution of each covariate to the near-surface O<sub>3</sub> (a), NO<sub>2</sub> (b), and  
 245 PM<sub>2.5</sub> (c) concentration quantified with the Shapley Additive explanations (SHAP)  
 246 method in the training dataset. The estimations of the model are shown above the  
 247 heatmap matrix and the global importance of each model input is shown as a bar plot  
 248 on the right side of the plot. The top fifteen variables of global importance are listed in  
 249 order from top to bottom. The abbreviation of “people\_density”, “road\_gau”, and  
 250 “land\_use” represents the people density, road density and land use data, respectively.  
 251 Another full form of the abbreviation can be found in Text S2 and Table S1.

252

**Table S1.** Summary of the dataset used in Air Transformer from multiple sources\*

Data category	Data name	Spatial resolution	Temporal resolution	Data source
Ground observation	O <sub>3</sub> 、NO <sub>2</sub> 、PM <sub>2.5</sub> measurements	Point	Hourly	<a href="http://www.sdem.org.cn">http://www.sdem.org.cn</a> <a href="http://www.cnemc.cn">http://www.cnemc.cn</a>
Satellite data	TROPOMI O <sub>3</sub> , NO <sub>2</sub> <sup>[1]</sup>	5.5 × 3.5 km <sup>[2]</sup>	Daily	<a href="https://scihub.copernicus.eu">https://scihub.copernicus.eu</a>
	MAIAC AOD <sup>[3]</sup>	1 × 1 km	Daily	<a href="https://lpdaac.usgs.gov/products/mcd19a2v006/">https://lpdaac.usgs.gov/products/mcd19a2v006/</a>
Meteorological fields	ERA5 <sup>[4]</sup>	0.25° × 0.25°	Hourly	<a href="https://cds.climate.copernicus.eu">https://cds.climate.copernicus.eu</a>
Ancillary data	Industry emission	Point	Hourly	<a href="http://www.sdem.org.cn">http://www.sdem.org.cn</a>
	Land use	30 × 30 m	-	<a href="http://www.globallandcover.com">http://www.globallandcover.com</a>
	People density	100m	-	<a href="https://hub.worldpop.org">https://hub.worldpop.org</a>
	Road density	0.5 × 0.5 km	-	<a href="https://www.openstreetmap.org">https://www.openstreetmap.org</a>
	Digital elevation model (DEM)	0.5 × 0.5 km	-	<a href="https://www.resdc.cn">https://www.resdc.cn</a>
	MODIS vegetation index <sup>[5]</sup>	0.25 × 0.25 km	16-daily	<a href="https://lpdaac.usgs.gov/products/mod13q1v061/">https://lpdaac.usgs.gov/products/mod13q1v061/</a>
	Nighttime lights (NTL)	0.5 × 0.5 km	Daily	<a href="https://ladsweb.modaps.eosdis.nasa.gov/missions-and-measurements/products/VNP46A2/">https://ladsweb.modaps.eosdis.nasa.gov/missions-and-measurements/products/VNP46A2/</a>
	Land surface temperature (LST)	1 × 1 km	Daily	<a href="https://e4ftl01.cr.usgs.gov">https://e4ftl01.cr.usgs.gov</a>
MERRA-2 AOD reanalysis <sup>[6]</sup>	0.625° × 0.5°	3-hourly	<a href="https://disc.gsfc.nasa.gov/datasets/M2I3NXGAS_5.12.4/summary">https://disc.gsfc.nasa.gov/datasets/M2I3NXGAS_5.12.4/summary</a>	
Spatial-temporal information	Euclidean spherical coordinates Temporal trend <sup>[7]</sup>	- -	- -	- -

254 \* The dataset covers the Shandong province of China from May 1, 2018 to July 1, 2021.

255 <sup>[1]</sup> TROPOMI satellite data contains: Tropospheric NO<sub>2</sub> column density (NO<sub>2</sub>); Total O<sub>3</sub> column density (O<sub>3</sub>); NO<sub>2</sub> slant columns density (NO<sub>2\_slant</sub>); Absorbing  
256 aerosol index (AAI); cloud fraction. The Level-2 data from TROPOMI were filtered based on quality assurance values (>0.5).

257 <sup>[2]</sup> 7.5 × 3.5 km from 30. May 2018 to 6. August 2019.

258 [3] MAIAC AOD data including Aerosol Optical Depth (AOD) and column water vapor over land and clouds (AOD\_cwv). The AOD was calculated by averaging the  
259 AOD at 0.47  $\mu\text{m}$  and 0.55  $\mu\text{m}$ . MAIAC AOD has better accuracy in the brighter areas<sup>15</sup> compared with AOD products generated from the Deep Blue<sup>16</sup> or Dark Target  
260 algorithms<sup>17</sup>.

261 [4] ERA5 hourly data on single levels (reanalysis). It contains 18 variables: 10 meter U wind component (u10), 10 meter V wind component (v10), 2 meter dewpoint  
262 temperature (d2m); 2 meter temperature (t2m); Boundary layer height (blh); Evaporation (e); Total precipitation (tp); Surface pressure (sp); Boundary layer dissipation;  
263 Cloud base height; Low vegetation cover; Forecast albedo; Instantaneous large-scale surface precipitation fraction; Medium cloud cover; Mean evaporation rate (mer);  
264 Mean surface downward long-wave radiation flux, clear sky (msdwlwrfcs); Mean surface downward short-wave radiation flux, clear sky (msdswrfcs); Mean sea level  
265 pressure (msl); Total columns ozone; Total columns water (tcw).

266 [5] MODIS vegetation index contains: Normalized Difference Vegetation Index (NDVI); Enhanced Vegetation Index (EVI).

267 [6] MERRA-2 AOD reanalysis contains: Aerosol Optical Depth Analysis, Aerosol Optical Depth Analysis Increment.

268 [7] Temporal trends contain: Helix-shape trigonometric month sequence; Julian day; Year; Month. One-hot encoding was used to process categorical variables.

269



270 **Table S2.** The performances of AiT in estimating multiple targeted pollutants as well as single  
 271 targeted pollutants. All four model was trained using the same input dataset, but different targets  
 272 (The targets of AiT is O<sub>3</sub>, NO<sub>2</sub>, PM<sub>2.5</sub>. The target of AiT\_O<sub>3</sub>, AiT\_NO<sub>2</sub>, AiT\_PM<sub>2.5</sub> is O<sub>3</sub>, NO<sub>2</sub> and  
 273 PM<sub>2.5</sub>, respectively).

Model	AiT			AiT_O <sub>3</sub>	AiT_NO <sub>2</sub>	AiT_PM <sub>2.5</sub>
	O <sub>3</sub>	NO <sub>2</sub>	PM <sub>2.5</sub>	O <sub>3</sub>	NO <sub>2</sub>	PM <sub>2.5</sub>
R <sup>2</sup>	0.96	0.92	0.90	0.97	0.92	0.90
RMSE (µg/m <sup>3</sup> )	9.96	4.72	11.99	9.27	4.75	12.57
MAE (µg/m <sup>3</sup> )	7.06	3.48	5.38	6.35	3.46	6.14

274

**Table S3.** Comparison of model performance with previous studies.

Model	Spatial resolution	Cross-validation		Pollutant	Literature
		R <sup>2</sup>	RMSE ( $\mu\text{g}/\text{m}^3$ )		
RF	0.05°	0.87	13.03	O <sub>3</sub>	Zhu et al., 2022 <sup>18</sup>
STET	0.1°	0.87	17.1	O <sub>3</sub>	Wei et al., 2022 <sup>19</sup>
LSTM	0.1°	0.94	10.64	O <sub>3</sub>	Wang et al., 2022 <sup>20</sup>
DP	0.003°	0.94	11.29	O <sub>3</sub>	Li et al., 2022 <sup>10</sup>
LightGBM	0.05°	0.91	14.14	O <sub>3</sub>	Wang et al., 2021 <sup>2</sup>
XGBoost	0.05°	0.83	7.58	NO <sub>2</sub>	Liu, 2021 <sup>21</sup>
LightGBM	0.05°	0.83	6.62	NO <sub>2</sub>	Wang et al., 2021 <sup>2</sup>
GTWR-SK	0.025°	0.84	6.70	NO <sub>2</sub>	Wu et al., 2021 <sup>22</sup>
FSDN	0.01°	0.82	8.80	NO <sub>2</sub>	Li & Wu, 2021 <sup>23</sup>
SWDF	0.01°	0.93	4.89	NO <sub>2</sub>	Wei et al., 2022 <sup>24</sup>
DP	0.04°	0.88	11.27	PM <sub>2.5</sub>	Song et al., 2022 <sup>1</sup>
DEML	0.01°	0.87	5.38	PM <sub>2.5</sub>	Yu et al., 2022 <sup>25</sup>
RF	0.1°	0.83	13.9–22.1	PM <sub>2.5</sub>	Geng et al., 2021 <sup>26</sup>
STET	0.01°	0.89	10.33	PM <sub>2.5</sub>	Wei et al., 2020 <sup>9</sup>
RF	0.01°	0.88	15.73	PM <sub>2.5</sub>	Huang et al., 2021 <sup>27</sup>
		0.90	15.5	O <sub>3</sub>	
RF*	0.005°	0.82	7.2	NO <sub>2</sub>	This study
		0.92	10.72	PM <sub>2.5</sub>	
		<b>0.96</b>	<b>10.11</b>	O <sub>3</sub>	
AiT	0.005°	<b>0.92</b>	<b>4.82</b>	NO <sub>2</sub>	This study
		<b>0.95</b>	<b>8.54</b>	PM <sub>2.5</sub>	

276 STET: Space-time extremely randomized trees; LSTM: Long short-term memory network; DP:  
 277 deep forest; semi-SILDLM: tree-based ensemble deep learning model; LightGBM: Light gradient  
 278 boosting machine; XGBoost: Extreme gradient boosting; GTWR-SK: Geographically and temporal  
 279 weighted regression with spatiotemporal kriging; SFDN: Full residual deep networks; SWDF:  
 280 Spatiotemporally weight deep forest; DEML: deep ensemble machine learning; RF: random forest;  
 281 AiT: Air Transformer.

282 \*: While training RF with variables involving neighboring grids is necessary, ML models are limited  
 283 to accepting only one-dimensional data. Flattening four-dimensional data ( $X \in R^{57 \times 8 \times 5 \times 5}$ ) causes  
 284 a significant increase in the number of features, which results in a reduction in model performance.  
 285 Thus, to ensure optimal performance, only variables in situ were employed to train RF.

286

287 **Table S4.** The average concentration of four pollutants across urban and non-urban areas in 2019  
 288 and 2020.

Year	Type	O <sub>3</sub>	NO <sub>2</sub>	PM <sub>2.5</sub>	HCHO
2019	Nonurban	141.1	24.7	33.3	3.5
	Urban	141.1	26.3	32.6	4.2
2020	Nonurban	129.2	24.2	30.8	3.3
	Urban	130.4	25.4	29.5	4.0
Relative Changes (%)	Nonurban	-8.43	-2.02	-7.51	-5.71
	Urban	-7.58	-3.42	-9.51	-4.76

289

## 290 References

- 291 (1) Song, Z.; Chen, B.; Zhang, P.; Guan, X.; Wang, X.; Ge, J.; Hu, X.; Zhang, X.; Wang, Y. High  
292 Temporal and Spatial Resolution PM<sub>2.5</sub> Dataset Acquisition and Pollution Assessment Based  
293 on FY-4A TOAR Data and Deep Forest Model in China. *Atmospheric Research* **2022**, *274*,  
294 106199. <https://doi.org/10.1016/j.atmosres.2022.106199>.
- 295 (2) Wang, Y.; Yuan, Q.; Li, T.; Zhu, L.; Zhang, L. Estimating Daily Full-Coverage near Surface  
296 O<sub>3</sub>, CO, and NO<sub>2</sub> Concentrations at a High Spatial Resolution over China Based on S5P-  
297 TROPOMI and GEOS-FP. *ISPRS Journal of Photogrammetry and Remote Sensing* **2021**, *175*,  
298 311–325. <https://doi.org/10.1016/j.isprsjprs.2021.03.018>.
- 299 (3) Lyapustin, A.; Wang, Y. MODIS/Terra+Aqua Land Aerosol Optical Depth Daily L2G Global  
300 1km SIN Grid V061. *NASA EOSDIS Land Processes DAAC* **2022**.  
301 <https://doi.org/10.5067/MODIS/MCD19A2.061>.
- 302 (4) Hersbach, H.; Bell, B.; Berrisford, G.; Horányi, A.; Muñoz Sabater, J.; Nicolas, J.; Peubey,  
303 C.; Rozum, I.; Schepers, D.; Simmons, A.; Soci, C.; Dee, D.; Thépaut, J.-N. ERA5 Hourly  
304 Data on Single Levels from 1959 to Present. *Copernicus Climate Change Service (C3S)*  
305 *Climate Data Store (CDS)* **2023**. <https://doi.org/10.24381/cds.adbb2d47>.
- 306 (5) Kim, M.; Brunner, D.; Kuhlmann, G. Importance of Satellite Observations for High-  
307 Resolution Mapping of near-Surface NO<sub>2</sub> by Machine Learning. *Remote Sensing of*  
308 *Environment* **2021**, *264*. <https://doi.org/10.1016/j.rse.2021.112573>.
- 309 (6) Sun, H.; Shin, Y. M.; Xia, M.; Ke, S.; Wan, M.; Yuan, L.; Guo, Y.; Archibald, A. T. Spatial  
310 Resolved Surface Ozone with Urban and Rural Differentiation during 1990–2019: A Space–  
311 Time Bayesian Neural Network Downscaler. *Environ. Sci. Technol.* **2022**, *56* (11), 7337–  
312 7349. <https://doi.org/10.1021/acs.est.1c04797>.
- 313 (7) Ke, G.; Meng, Q.; Finley, T.; Wang, T.; Chen, W.; Ma, W.; Ye, Q.; Liu, T.-Y. LightGBM: A  
314 Highly Efficient Gradient Boosting Decision Tree. *Advances in Neural Information*  
315 *Processing Systems 30* **2017**, 3149–3157.
- 316 (8) Zang, Z.; Guo, Y.; Jiang, Y.; Zuo, C.; Li, D.; Shi, W.; Yan, X. Tree-Based Ensemble Deep  
317 Learning Model for Spatiotemporal Surface Ozone (O<sub>3</sub>) Prediction and Interpretation.  
318 *International Journal of Applied Earth Observation and Geoinformation* **2021**, *103*, 102516.  
319 <https://doi.org/10.1016/j.jag.2021.102516>.
- 320 (9) Wei, J.; Li, Z.; Cribb, M.; Huang, W.; Xue, W.; Sun, L.; Guo, J.; Peng, Y.; Li, J.; Lyapustin,  
321 A.; Liu, L.; Wu, H.; Song, Y. Improved 1 Km Resolution PM<sub>2.5</sub> Estimates across China Using  
322 Enhanced Space–Time Extremely Randomized Trees. *Atmos. Chem. Phys.* **2020**, *20* (6),  
323 3273–3289. <https://doi.org/10.5194/acp-20-3273-2020>.
- 324 (10) Li, M.; Yang, Q.; Yuan, Q.; Zhu, L. Estimation of High Spatial Resolution Ground-Level  
325 Ozone Concentrations Based on Landsat 8 TIR Bands with Deep Forest Model. *Chemosphere*  
326 **2022**, *301*, 134817. <https://doi.org/10.1016/j.chemosphere.2022.134817>.
- 327 (11) Liu, X.; He, P.; Chen, W.; Gao, J. Multi-Task Deep Neural Networks for Natural Language  
328 Understanding. arXiv May 29, 2019. <http://arxiv.org/abs/1901.11504> (accessed 2022-11-22).
- 329 (12) Su, W.; Hu, Q.; Chen, Y.; Lin, J.; Zhang, C.; Liu, C. Inferring Global Surface HCHO  
330 Concentrations from Multisource Hyperspectral Satellites and Their Application to HCHO-  
331 Related Global Cancer Burden Estimation. *Environment International* **2022**, *170*, 107600.  
332 <https://doi.org/10.1016/j.envint.2022.107600>.

- 333 (13) Cooper, M. J.; Martin, R. V.; McLinden, C. A.; Brook, J. R. Inferring Ground-Level Nitrogen  
334 Dioxide Concentrations at Fine Spatial Resolution Applied to the TROPOMI Satellite  
335 Instrument. *Environ. Res. Lett.* **2020**, *15* (10), 104013. [https://doi.org/10.1088/1748-](https://doi.org/10.1088/1748-9326/aba3a5)  
336 [9326/aba3a5](https://doi.org/10.1088/1748-9326/aba3a5).
- 337 (14) Inness, A.; Ades, M.; Agustí-Panareda, A.; Barré, J.; Benedictow, A.; Blechschmidt, A.-M.;  
338 Dominguez, J. J.; Engelen, R.; Eskes, H.; Flemming, J.; Huijnen, V.; Jones, L.; Kipling, Z.;  
339 Massart, S.; Parrington, M.; Peuch, V.-H.; Razinger, M.; Remy, S.; Schulz, M.; Suttie, M.  
340 The CAMS Reanalysis of Atmospheric Composition. *Atmos. Chem. Phys.* **2019**, *19* (6), 3515–  
341 3556. <https://doi.org/10/ghdkrm>.
- 342 (15) Lyapustin, A.; Wang, Y.; Laszlo, I.; Kahn, R.; Korkin, S.; Remer, L.; Levy, R.; Reid, J. S.  
343 Multiangle Implementation of Atmospheric Correction (MAIAC): 2. Aerosol Algorithm.  
344 *Journal of Geophysical Research: Atmospheres* **2011**, *116* (D3).  
345 <https://doi.org/10.1029/2010JD014986>.
- 346 (16) Hsu, N. C.; Jeong, M.-J.; Bettenhausen, C.; Sayer, A. M.; Hansell, R.; Seftor, C. S.; Huang,  
347 J.; Tsay, S.-C. Enhanced Deep Blue Aerosol Retrieval Algorithm: The Second Generation.  
348 *Journal of Geophysical Research: Atmospheres* **2013**, *118* (16), 9296–9315.  
349 <https://doi.org/10.1002/jgrd.50712>.
- 350 (17) Kaufman, Y. J.; Wald, A. E.; Remer, L. A.; Gao, B.-C.; Li, R.-R.; Flynn, L. The MODIS 2.1-  
351 /Spl Mu/m Channel-Correlation with Visible Reflectance for Use in Remote Sensing of  
352 Aerosol. *IEEE Transactions on Geoscience and Remote Sensing* **1997**, *35* (5), 1286–1298.  
353 <https://doi.org/10.1109/36.628795>.
- 354 (18) Zhu, Q.; Bi, J.; Liu, X.; Li, S.; Wang, W.; Zhao, Y.; Liu, Y. Satellite-Based Long-Term  
355 Spatiotemporal Patterns of Surface Ozone Concentrations in China: 2005–2019. *Environ*  
356 *Health Perspect* **2022**, *130* (2), 027004. <https://doi.org/10.1289/EHP9406>.
- 357 (19) Wei, J.; Li, Z.; Li, K.; Dickerson, R. R.; Pinker, R. T.; Wang, J.; Liu, X.; Sun, L.; Xue, W.;  
358 Cribb, M. Full-Coverage Mapping and Spatiotemporal Variations of Ground-Level Ozone  
359 (O<sub>3</sub>) Pollution from 2013 to 2020 across China. *Remote Sensing of Environment* **2022**, *270*,  
360 112775. <https://doi.org/10.1016/j.rse.2021.112775>.
- 361 (20) Wang, S.; Mu, X.; Jiang, P.; Huo, Y.; Zhu, L.; Zhu, Z.; Wu, Y. New Deep Learning Model to  
362 Estimate Ozone Concentrations Found Worrying Exposure Level over Eastern China.  
363 *International Journal of Environmental Research and Public Health* **2022**, *19* (12), 7186.  
364 <https://doi.org/10.3390/ijerph19127186>.
- 365 (21) Liu, J. Mapping High Resolution National Daily NO<sub>2</sub> Exposure across Mainland China Using  
366 an Ensemble Algorithm. *Environmental Pollution* **2021**, *279*, 116932.  
367 <https://doi.org/10.1016/j.envpol.2021.116932>.
- 368 (22) Wu, S.; Huang, B.; Wang, J.; He, L.; Wang, Z.; Yan, Z.; Lao, X.; Zhang, F.; Liu, R.; Du, Z.  
369 Spatiotemporal Mapping and Assessment of Daily Ground NO<sub>2</sub> Concentrations in China  
370 Using High-Resolution TROPOMI Retrievals. *Environmental Pollution* **2021**, *273*, 116456.  
371 <https://doi.org/10.1016/j.envpol.2021.116456>.
- 372 (23) Li, L.; Wu, J. Spatiotemporal Estimation of Satellite-Borne and Ground-Level NO<sub>2</sub> Using Full  
373 Residual Deep Networks. *Remote Sensing of Environment* **2021**, *254*, 112257.  
374 <https://doi.org/10.1016/j.rse.2020.112257>.
- 375 (24) Wei, J.; Liu, S.; Li, Z.; Liu, C.; Qin, K.; Liu, X.; Pinker, R. T.; Dickerson, R. R.; Lin, J.;  
376 Boersma, K. F.; Sun, L.; Li, R.; Xue, W.; Cui, Y.; Zhang, C.; Wang, J. Ground-Level NO<sub>2</sub>

- 377 Surveillance from Space Across China for High Resolution Using Interpretable  
378 Spatiotemporally Weighted Artificial Intelligence. *Environ. Sci. Technol.* **2022**,  
379 acs.est.2c03834. <https://doi.org/10.1021/acs.est.2c03834>.
- 380 (25) Yu, W.; Li, S.; Ye, T.; Xu, R.; Song, J.; Guo, Y. Deep Ensemble Machine Learning  
381 Framework for the Estimation of PM<sub>2.5</sub> Concentrations. *Environ Health Perspect* **2022**, *130*  
382 (3), 037004. <https://doi.org/10.1289/EHP9752>.
- 383 (26) Geng, G.; Xiao, Q.; Liu, S.; Liu, X.; Cheng, J.; Zheng, Y.; Xue, T.; Tong, D.; Zheng, B.; Peng,  
384 Y.; Huang, X.; He, K.; Zhang, Q. Tracking Air Pollution in China: Near Real-Time PM<sub>2.5</sub>  
385 Retrievals from Multisource Data Fusion. *Environ. Sci. Technol.* **2021**, *55* (17), 12106–12115.  
386 <https://doi.org/10.1021/acs.est.1c01863>.
- 387 (27) Huang, C.; Hu, J.; Xue, T.; Xu, H.; Wang, M. High-Resolution Spatiotemporal Modeling for  
388 Ambient PM<sub>2.5</sub> Exposure Assessment in China from 2013 to 2019. *Environ. Sci. Technol.*  
389 **2021**, *55* (3), 2152–2162. <https://doi.org/10.1021/acs.est.0c05815>.
- 390